A semiautomated approach for artefact removal in serial tissue cryosections

L.M. KINDLE*, I.A. KAKADIARIS†, T. JU‡ & J.P. CARSON*

Biological Monitoring and Modeling Group, Pacific Northwest National Laboratory, Richland, Washington, U.S.A.

†*Computational Biomedicine Laboratory, Department of Computer Science, University of Houston, Houston, Texas, U.S.A.*

‡*Department of Computer Science and Engineering, Washington University in St. Louis, St. Louis, Missouri, U.S.A.*

Summary

Thinly sliced serial tissue sections of an organ can be imaged using optical microscopy at a resolution detailing individual cells. When the tissue sections are first subjected to *in situ* hybridization or immunohistochemistry, these data sets can be analysed for changes in gene expression and gene products. Such spatial information is important for understanding the functional effects of experimental or environmental challenges to the organism. However, a critical step in analysing these data sets is mitigating artefacts that result from the preparation of the tissue sections. In this paper, we describe an automated method with manual validation tools that together enable detecting and addressing artefacts including dust particles and air bubbles.

Introduction

Bioimage informatics is an emerging field requiring application of biological knowledge to data-intensive problems (Peng, 2008). The field includes digitally imaged histology, which is increasingly being utilized to generate quantitative data, thus escalating the amount of information available at an accelerating rate. An example of this is high throughput *in situ* hybridization for the collection of spatial gene expression data (Visel *et al.*, 2004). With this approach, gene expression can be quantified throughout an organ or organism at cellular resolution (Carson *et al.*, 2005a; Lee *et al.*, 2008). This is a powerful method not only for detecting functional changes caused by the experimental environment of the organism studied, but also for learning more about the biological mechanisms involved in these functional changes. Such is the

impact of these histological images that spatially normalized atlas-based databases have been developed to store quantified gene expression information from images of a mouse brain (Carson *et al.*, 2005b; Bello *et al.*, 2007; Lein *et al.*, 2007; Ju *et al.*, 2010).

The basic approach for digital histology of the whole mouse brain relies on thin serial sectioned tissue, *in situ* hybridization staining, digital imaging and digital analysis of the stains (Carson *et al.*, 2002). Despite the impact of these histological databases, there has been little description of the necessary steps required to ensure that the digital data are free of artefacts and thus accurately represent the quantitative spatial distribution of gene expression. Such accuracy becomes increasingly important as this type of histological data moves beyond databases and begins to be used for quantitative assessment of changes in gene expression (McGill *et al.*, 2006; Yaylaoglu *et al.*, 2006; Fyffe *et al.*, 2008; Gatchel *et al.*, 2008; Ben-Shachar *et al.*, 2009).

Speed and reliability in image processing are essential requirements for the analysis of large-scale imaging data. Although the described serial tissue sectioning procedure has the advantage over other imaging methods, such as MRI, of being able to visualize individual cells, tissue section preparation approaches can produce artefacts in the data. Tissue deformations – stretching and compactions – have been addressed in previous publications (Ju *et al.*, 2003, 2006). For the purpose of this paper, the term artefact will refer to substances not naturally present such as dust particles and air bubbles. These artefacts can be misinterpreted as cells expressing a gene of interest, thus preventing the rapid and accurate detection of gene expression in the tissue. Therefore, a critical step in generating accurate quantitative data is the mitigation of artefacts incurred during the tissue section preparation process. Although a manual removal of the artefacts in the image is one potential solution,

Correspondence to: Dr. James Carson, Biological Monitoring and Modeling Group, Pacific Northwest National Laboratory, Richland, WA, U.S.A. Tel: +1-509-3716894; fax: +1-509-3716978; e-mail: james.carson@pnl.gov

relying exclusively on manual operations takes a substantial amount of time and requires a knowledgeable operator who can discern the defects from the gene expression as well as an understanding of how to best to mitigate artefacts without compromising the scientific integrity of the analysis. To ameliorate the process of artefact mitigation, we have developed a set of algorithms and tools including a graphical user interface (GUI) that semiautomates the process of removing artefacts. The goal of the toolkit is to facilitate application and validation of automated algorithms that identify and mitigate artefacts in the given set of images representing serial tissue sections. The underlying principle for automated artefact detection is to calculate unexpected differences between a specified image and its neighbouring images by first warping neighbouring images to match the shape of the specified image. We detail herein this approach.

Materials and methods

The fundamental steps for automatically detecting artefacts are data collection, tissue tear repair, image registration with neighbouring images and comparing the image to registered neighbouring images. These steps are outlined in Fig. 1 and detailed herein.

Image data collection

The image data utilized was collected from a serial set of thin tissue sections of the mouse brain as previously described in another study (McGill *et al.*, 2006). In summary, a mouse brain was frozen in a block of OCT and thinly sliced into 448 serial coronal sections each 25 μm thick. Parallelized, high-throughput robotic *in situ* hybridization using digoxygenin-tagged riboprobes was then performed on all of the sections using a probe for *corticotropin-releasing hormone*. The epitope-tagged probes are visualized as a blue/purple signal through a two-step amplification reaction involving catalytic reporter deposition and an enzymatic colour reaction (Kerstens *et al.*, 1995). This approach has a level of sensitivity comparable to that provided by radioactive labelling. A CCD camera-equipped microscope then digitized expression data from each tissue section using an automated stage to record the entire section at 1.6 μm per pixel (Carson *et al.*, 2002).

Tissue tear repair

Tears occurring during the physical slicing of the tissue tended to form in a direction perpendicular to the slicing motion. Slicing was performed in a bottom to top direction. Therefore, the vast majority of tears in the coronal tissue section image appear as horizontal tears. An example of a tissue section with two tears is shown in Fig. 2(a). Tears dynamically stretch the tissue above or below the tear, depending on the orientation of the tissue during sectioning. Undoing the effects of the tear involves reversing this stretching. The approach for fixing tears is to first identify the area of the tear, calculate a smoothed tear outline and then apply a repair algorithm to undo the effects of the tear. As the dorsal–ventral orientation of the tissue within the frozen block during sectioning may be unknown, the tear repair algorithm brings the tissue both at the top and bottom of the tear together. It accomplishes this by first determining the points outlining of the top of the tear. This outline is smoothed by calculating the average height of the points defining the top of the tear using a running window size of 21. The averaged outline is further smoothed by limiting the point-wise slope to between −1 and 1. The smoothed outline of the tear bottom is calculated by the same protocol. Using the smoothed tear outline, each column of the image containing the tear is modified in the following way. The location within the tear halfway between the top of the tear and bottom of the tear as defined by the smoothed outlines is set as the middle of the tear for that column of the image. Then, the image column from the top of the smoothed outline to the top of the image is linearly stretched to occupy the pixels from
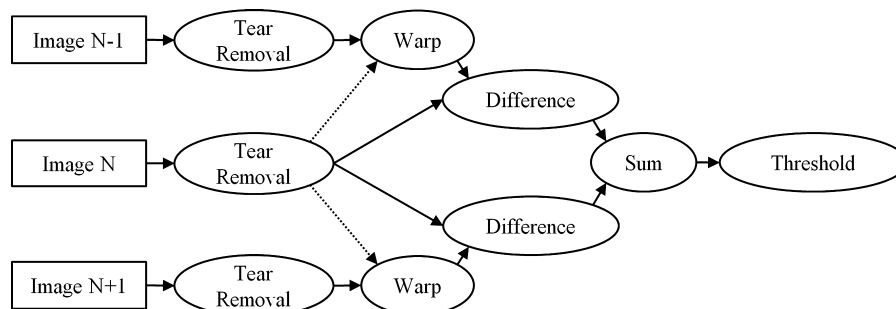

Fig. 1. Overview of automated artefact detection in a given image. After data collection and digitization, significant tears are removed from the image and its nearest neighbouring images. Next, the neighbouring images are warped to match the shape of the image and the pixel-by-pixel intensity differences are calculated. After applying local averaging, the intensity differences are summed and an intensity threshold is applied to indicate the areas of the image likely to contain artefacts.
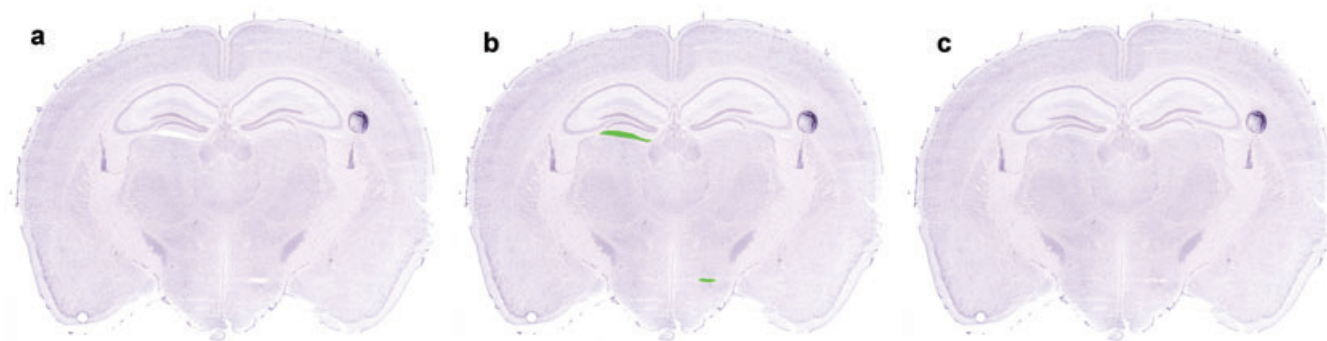
Fig. 2. Semiautomated tear fixing. (a) Example tissue section image with two tears caused by thin cryosection production. (b) Area of tears manually indicated in green using GUI tools: fill, draw and erase. (c) Indicated tears are automatically removed from the image using a process that dynamically stretches the image above and below the tear to close the gap.

the middle of the tear to the top of the image. Similarly, the image column from the bottom of the smoothed outline to the bottom of the image is linearly stretched to occupy the pixels from the middle of the tear to the bottom of the image.

Image registration

Our approach for detecting false positive signal artefacts in an image relies upon locating the regions of common differences between the image and its two neighbouring images, that is the two images representing the tissue sections acquired immediately previous and after the tissue section represented in the current image. To make this comparison, nonlinear registration was performed upon the two neighbouring images to bring them into direct alignment with the image being analysed. This registration process of transforming the images to the same shape and coordinates was performed via three steps: image preparation, rigid alignment and elastic alignment.

Image preparation consisted of first reducing the image to 12.5% of the original size (reduced size: $\sim$745 $\times$ 582 pixels) to speed up alignment calculations. Then, to remove the effect of the image background intensity during registration, background normalization was performed to adjust the image background pixels to white intensity (i.e. 255). This normalization was based on a threshold t that accounted for 90% of the pixels in the four corners of the image defined by square regions each 50 $\times$ 50 pixels in size. To normalize the background, the intensity of each pixel in the image was multiplied by $\frac{255}{t}$, then limited to a maximum new value of 255. Next, the image canvas was expanded to 1088 $\times$ 832 pixels to establish a common image size for all of the images and prevent the interference of image boundaries during image rotations and translations.

Rigid alignment first searched for the set of horizontal and vertical image translations in addition to image rotations that would best align adjacent images. Each potential alignment was scored by minimizing the sum of pixel-to-pixel intensity

differences between the two images. The algorithm performed the rigid transformations at multiple image scales to speed up the search process. The rigid alignment with the minimum score was applied.

Elastic alignment was performed using the ImageJ (Rasband, 1997–2010) software plug-in bUnwarpJ (Arganda-Carreras *et al.*, 2006). bUnwarpJ calculated and applied optimized warp transformations between rigidly aligned images. We utilized the following bUnwarpJ settings: registration = Accurate, image_subsample_factor = 1, initial_deformation = Coarse, final_deformation = Very Fine, divergence_weight = 0.1, curl_weight = 0.1, landmark_ weight = 0, image_weight = 1.0, consistency_weight = 1.0, stop_threshold = 0.01.

Artefact detection

The strategy of automated false positive signal detection is based upon the likelihood that an artefact, such as a dust particle, will not appear in consecutive tissue sections in the same place. By contrast, desirable image features, such as gene expression, tend to appear in adjacent images. The process of this artefact detection is illustrated with an example in Fig. 3. Detection of artefacts in a particular image of a tissue section from a set of series sections (Fig. 3b) relies upon the image representing the preceding tissue section (Fig. 3a) and the image representing the next tissue section (Fig. 3c). First, the image registration process described earlier is applied to register the preceding image (Fig. 3d) and the next image (Fig. 3e) with the current image. The pixel-to-pixel absolute intensity difference image is then calculated for the preceding image to current image (Fig. 3f) and for the next image to current image (Fig. 3g). These two difference images highlight both the regions of potential artefacts in the current image but also artefacts in the adjacent image. By summing the two difference images (Fig. 3h), the artefacts in the current image effectively double in intensity while artefacts in adjacent images do not change. As a final step, a series of thresholds are
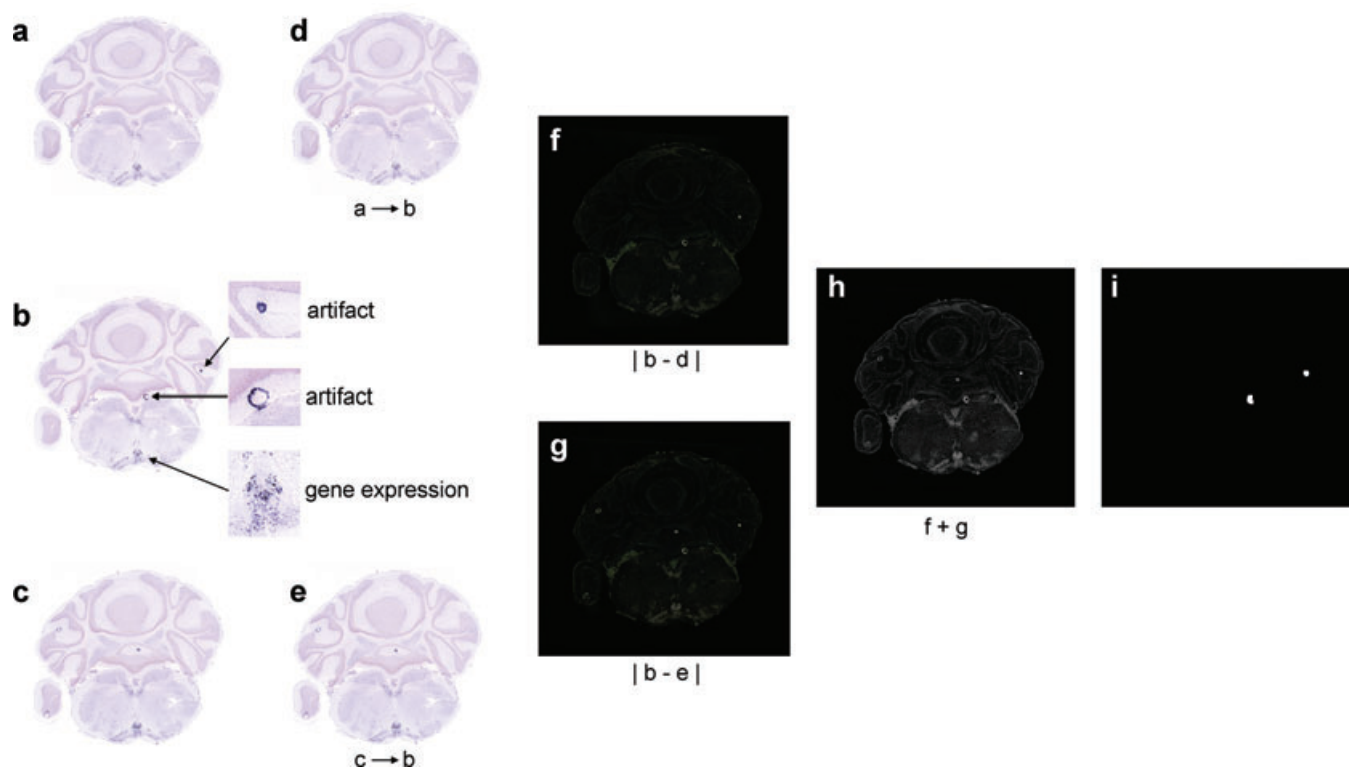
Fig. 3. Illustrated application of automated artefact detection. (a–c) A sequential series of three images with tears already removed, with artefact detection focused on image (b). Insets highlight the two artefacts to detect as well as example of gene expression, which should not be detected as an artefact. (d) The image (a) elastically registered to match the shape of image (b). (e) The image (c) elastically registered to match the shape of image (b). (f) The pixel-by-pixel absolute difference in grey-scale intensity between the images in (b) and (d). (g) The pixel-by-pixel absolute difference in intensity between the images in (b) and (e). (h) The pixel-by-pixel intensity sum of the images in (f) and (g). (i) A binary mask indicated location of artefacts is derived from (h) using a series of filters described in the text.

then applied to generate the binary image mask that indicates the automatically detected artefacts in the current image (Fig. 3i). This final step also assists in preventing false positives caused by small cell-to-cell differences in gene expression. The final thresholding process begins by setting intensity values of 254 and 255 to be white (i.e. 255), and intensities of 0–253 to be black (i.e. 0). A Gaussian blur of radius 2 was then applied using Python Image Library's BLUR filter. This was followed by two utilizations of MaxFilter, which replaces the pixel with the maximum pixel intensity value in a 5×5 window. Finally, a threshold was used to binarize the image by setting pixels of intensity 50 and above to white (i.e. 1) and pixels below 50 to black (i.e. 0). White pixels in this mask indicate the automatically detected artefacts.

Deftekt toolkit

A GUI called the Deftekt Toolkit was developed in Tk and Python to facilitate the application of the described automated processing steps and integrate the manual interactive capabilities. Manual interactive capabilities for tear fixing include the ability to indicate tear locations with standard draw, erase and fill tools. The toolkit includes the automated scripts for image registration that can be applied to all images within a folder, as well as automated scripts for detecting artefacts. The GUI allows the artefact mask to then be manually augmented as necessary. In this way, the toolkit streamlines the workflow for addressing any issues arising in tissue section images.

Results

The success of the artefact detection method is illustrated in four representative tissue section images (Fig. 4). The original tissue sections with tissue tears already repaired are shown in Figs 4(a)–(d) with insets highlighting all 11 tissue section artefacts of significance. These vary in size, shape and intensity. Seven artefacts are dark, like gene expression, and four are lighter intensity, like unexpressed tissue. Two artefacts are small dots approximately the size of a cell body, eight are larger circles and one is stringy. Figure 4(e)–(h) displays in red the automatically detected artefact mask for all four images. Also shown is the Deftekt GUI toolkit interface. The automated detection successfully identifies all of the dark
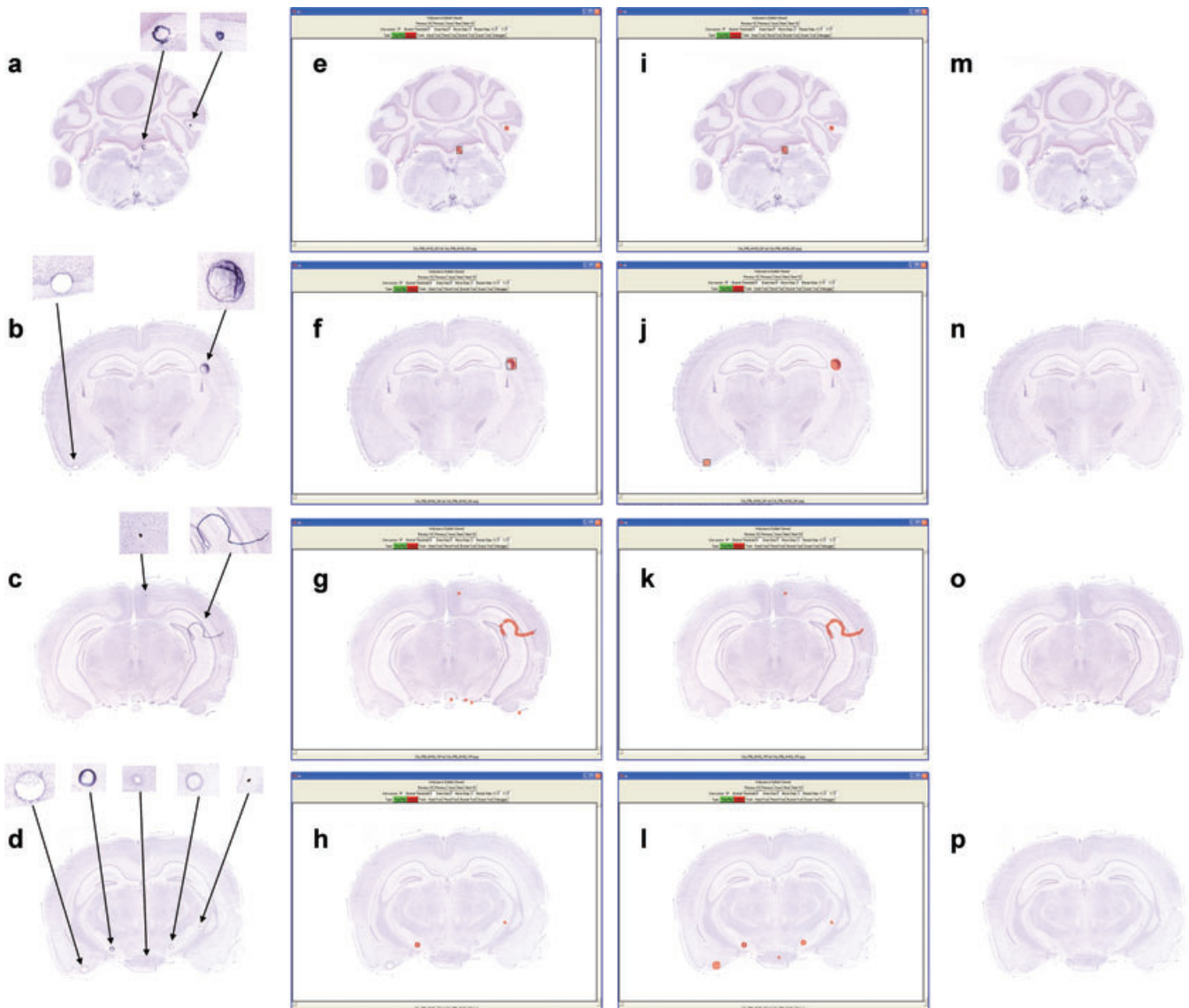
Fig. 4. Comparison of automated and manual artefact detection. (a–d) Four example tissue sections with all significant artefacts highlighted. (e–h) Red regions indicate automatically detected artefacts for the four images, shown with the GUI interface for making modifications to the detected mask. (i–l) Red regions have been modified in the four images to in some cases reshape artefact boundaries, remove false positives, and add additional artefact masks where artefacts were not automatically detected. (m–p) Optional artefact mitigation step uses the artefact mask definition and a neighbouring elastically registered image to automatically remove the artefacts from the image.

intensity artefacts including dots, circles and strings. Tissue artefacts with light intensity are not automatically detected. Several false positives are identified in one of the images just outside the perimeter of the tissue (Fig. 4g) The artefact mask is finalized through a manual process using the Deftekt GUI tools to remove, add and/or modify the locations indicating artefacts (Figs 4(i)–(l)). Through this approach, all significant artefacts are indicated in the mask. The resulting images from applying the optional tissue repair function are shown in Figs 4(m)–(p). In these repaired images, all artefacts have been removed without impacting gene expression or cellular density information.

Automated steps can be run overnight for a complete mouse brain data set (~450 images) on a standard desktop workstation (3Ghz dual core, 3GB RAM). Based on performance results, using the Deftekt GUI approach would likely reduce manpower time from 3 weeks to less than 1 week for a complete dataset.

Discussion

We have developed and demonstrated an approach for identifying and mitigating artefacts that can interfere with analysis of gene expression highlighted in tissue sections. The

approach combines automated steps and manual validation in a toolkit to enable streamlined processing of images. The immediate impact of this method is to decrease the amount of time required in handling artefacts, thus enabling more applications of *in situ* hybridization gene expression in tissue sections. These applications include quantitative analysis of gene expression both for comparison between specimens collected under different experiments, and for querying databases of spatial gene expression. The described approach is not limited to mouse brain, gene expression images or even tissue sections, but may be potentially applicable to any serial collection of 2D images from a 3D object where distortion can occur and individual image artefacts need to be identified and/or removed. Limitations include that the described tear removal approach performs best with tears that are horizontal and smooth. Undesirable warping of the image while fixing the tear is avoided by limiting the change in shift from one column to the next. However, multiple tears occurring within the same image column can increase the distortion. Future work in this area may include an automated tear detection algorithm. The approach and toolkit provide the foundation for future development in the domain of artefact detection. New algorithms that are developed can be easily integrated into the toolkit for testing and comparison with other approaches.

Corticotropin-releasing hormone expression patterns in mouse brain tissue sections consist of both scattered and regional elements, as well as both weak and strong expression patterns. For this reason, *corticotropin-releasing hormone* is a good gene to demonstrate the capability of the artefact detection approach. Performing image registration and tear repair prior to comparing neighbouring images results in improved alignment both for anatomical regions and for cell populations with *corticotropin-releasing hormone* expressed. In addition, the first appearance of gene expression in an anatomical region is not detected as an artefact because at least one neighbour should also show that gene expression. This is because regionalized gene expression generally extends across multiple images. Thresholds were empirically selected so that an artefact in a neighbouring image is not detected as an artefact in the current image. It is possible that the selected thresholds may be optimized further for other genes and their expression patterns. One limitation of approach as currently implemented is that dark artefacts are more readily detected. However, it is the dark artefacts that are the most important artefacts to detect because the quantification of gene expression relies on detecting dark cell-sized features.

Acknowledgements

References

Arganda-Carreras, I., Sanchez, C.O., Marabini, R., Carazo, J.M., Ortiz-de Solorzano, C. & Kybic, J. (2006) Consistent and elastic registration of histological sections using vector-spline regularization. *Lect. Notes Comput. Sci. – Comput. Vis. Approaches Med. Image Anal.* **4241**, 85–95.

Bello, M., Ju, T., Carson, J., Warren, J., Chiu, W. & Kakadiaris, I.A. (2007) Learning-based segmentation framework for tissue images containing gene expression data. *IEEE Trans. Med. Imaging* **26**, 728–744.

Ben-Shachar, S., Chahrour, M., Thaller, C., Shaw, C.A. & Zoghbi, H.Y. (2009) Mouse models of MeCP2 disorders share gene expression changes in the cerebellum and hypothalamus. *Hum. Mol. Genet.* **18**, 2431–2442.

Carson, J.P., Eichele, G. & Chiu, W. (2005a) A method for automated detection of gene expression required for the establishment of a digital transcriptome-wide gene expression atlas. *J. Microsc.* **217**, 275–281.

Carson, J.P., Ju, T., Lu, H.C., *et al.* (2005b) A digital atlas to characterize the mouse brain transcriptome. *PLoS Comput. Biol.* **1**, e41.

Carson, J.P., Thaller, C. & Eichele, G. (2002) A transcriptome atlas of the mouse brain at cellular resolution. *Curr. Opin. Neurobiol.* **12**, 562–565.

Fyffe, S.L., Neul, J.L., Samaco, R.C., *et al.* (2008) Deletion of Mecp2 in Sim1-expressing neurons reveals a critical role for MeCP2 in feeding behavior, aggression, and the response to stress. *Neuron* **59**, 947–958.

Gatchel, J.R., Watase, K., Thaller, C., *et al.* (2008) The insulin-like growth factor pathway is altered in spinocerebellar ataxia type 1 and type 7. *Proc. Natl. Acad. Sci. USA* **105**, 1291–1296.

Ju, T., Carson, J., Liu, L., Warren, J., Bello, M. & Kakadiaris, I. (2010) Subdivision meshes for organizing spatial biomedical data. *Methods* **50**, 70–76.

Ju, T., Warren, J., Carson, J., Bello, M., Kakadiaris, I., Chiu, W., Thaller, C. & Eichele, G. (2006) 3D volume reconstruction of a mouse brain from histological sections using warp filtering. *J. Neurosci. Methods* **156**, 84–100.

Ju, T., Warren, J., Eichele, G., Thaller, C., Chiu, W. & Carson, J. (2003) A geometric database for gene expression data. In: *Eurographics Symposium on Geometry Processing* (ed. by L. Kobbelt, P. Schröder & H. Hoppe). Eurographics Association, Aachen, Germany.

Kerstens, H.M., Poddighe, P.J. & Hanselaar, A.G. (1995) A novel in situ hybridization signal amplification method based on the deposition of biotinylated tyramine. *J. Histochem. Cytochem.* **43**, 347–352.

Lee, C.K., Sunkin, S.M., Kuan, C., *et al.* (2008) Quantitative methods for genome-scale analysis of in situ hybridization and correlation with microarray data. *Genome Biol.* **9**, R23.

Lein, E.S., Hawrylycz, M.J., Ao, N., *et al.* (2007) Genome-wide atlas of gene expression in the adult mouse brain. *Nature* **445**, 168–176.

McGill, B.E., Bundle, S.F., Yaylaoglu, M.B., Carson, J.P., Thaller, C. & Zoghbi, H.Y. (2006) Enhanced anxiety and stress-induced

corticosterone release are associated with increased Crh expression in a mouse model of Rett syndrome. *Proc. Natl. Acad. Sci. USA* **103**, 18267–18272.

Peng, H. (2008) Bioimage informatics: a new area of engineering biology. *Bioinformatics* **24**, 1827–1836.

Rasband, W.S. (1997–2010) ImageJ. U.S. National Institutes of Health, Maryland.

Visel, A., Thaller, C. & Eichele, G. (2004) Genepaint.org: an atlas of gene expression patterns in the mouse embryo. *Nucleic Acids Res.* **32**, D552–D556.

Yaylaoglu, M.B., Agbemafle, B.M., Oesterreicher, T.J., Finegold, M.J., Thaller, C. & Henning, S.J. (2006) Diverse patterns of cell-specific gene expression in response to glucocorticoid in the developing small intestine. *Am. J. Physiol.* **291**, G1041–G1050.